Reverse-Correlation Analysis of the Mechanosensation Circuit and Behavior in *C. elegans* Reveals Temporal and Spatial Encoding

Daniel A. Porto[1], John Giblin[2], Yiran Zhao[2], Hang Lu[1,2,3*]

[1]Interdisciplinary Bioengineering Program, Georgia Institute of Technology, USA

[2]Department of Biomedical Engineering, Georgia Institute of Technology, USA

[3]School of Chemical & Biomolecular Engineering, Georgia Institute of Technology, USA

*Correspondence should be addressed to HL: hang.lu@gatech.edu, 1-404-894-8473

Abstract

Animals must integrate the activity of multiple mechanoreceptors to navigate complex environments. In *Caenorhabditis elegans*, the general roles of the mechanosensory neurons have been defined, but most studies involve end-point or single-time-point measurements, and thus lack dynamical information. Here, we formulate a set of unbiased quantitative characterizations of the mechanosensory system by using reverse correlation analysis on behavior. We use a custom tracking, selective illumination, and optogenetics platform to compare two mechanosensory systems: the gentle-touch (TRNs) and harsh-touch (PVD) circuits. This method yields characteristic linear filters that allow for prediction of behavioral responses. The resulting filters are consistent with previous findings, and further provide new insights on the dynamics and spatial encoding of the systems. Our results suggest that the tiled network of the gentle-touch neurons has better resolution for spatial encoding than the harsh-touch neurons. Additionally, linear-nonlinear models can predict behavioral responses based only on sensory neuron activity. Our results capture the overall dynamics of behavior induced by the activation of sensory neurons, providing simple transformations that quantitatively characterize these systems. Furthermore, this platform can be extended to capture the behavioral dynamics induced by any neuron or other excitable cells in the animal.

Introduction

A key function of the nervous system is to integrate the activity from a variety of sensory neurons and transform these neuronal signals into specific behavioral responses. This integration occurs not only across sensory modalities but also spatially and temporally within a single modality such as in mechanosensation [1]. Characterizations of how the nervous system processes this information is vital for understanding brain function and allowing for prediction of behavioral responses. *Caenorhabditis elegans*, a nematode with a mapped connectome and powerful genetic and physiology tools, is an effective model organism for investigating relationships between sensory inputs and downstream

activities [2,3]. The components of the neural circuits involved in *C. elegans* mechanosensation have been elucidated through various genetic and behavioral analyses, coupled with neuronal cell ablation assays [4–6]. Two sets of mechanoreceptors are specifically responsible for sensing touch throughout the body: the gentle touch sensing TRNs and harsh touch sensing PVDs [7]. These specific neurons have been the focus of a number of studies, including genetic dissections of the mechanical signal transduction, their calcium responses and the eventual behavioral outcomes [4,8–15]. However, most descriptions are specific to a single specific input stimulus, typically a single pulse with an eye lash or a metal pick, and a single behavioral output. This leaves unexplored space of the stimuli and outputs, leading to descriptions that are potentially biased toward a specific stimulus, and not allowing for the generalizable prediction of the system.

To map the transformations between mechanoreceptor neurons and behavioral outputs, we sought to model these transformations in an unbiased quantitative framework that captures the systems' dynamics in a predictive manner. This is computationally challenging because of the stochasticity and complexity of the animal's behavioral repertoire, as well as the various time scales and frequencies relevant in the system[16–18]. A successful technique for characterizing neuronal systems is the use of reverse correlation analysis with a white noise stimulus [19–26]. This methodology is commonly applied in sensory physiology to model a sensory neuron's response to natural stimuli as a linear filter. The computed linear filters provide a complete description of the linear dynamics of the neuron, and can be used in conjunction with a nonlinear filter to accurately model its function [21,27–30]. This technique has also been extended to modeling sensory neurons[31] and behavior in invertebrates[32–36]. However, this technique has not been extended to model and contrast the spatial and temporal properties of behavioral responses to the gentle and harsh touch mechanosensory neurons.

Although reverse correlation analysis allows for accurate estimations of system dynamics, several experimental obstacles hinder its applicability to the mechanosensory circuits in *C. elegans* at present.

71 Current techniques for delivering precise mechanical stimuli to animals involve the delivery of a
72 mechanical force via a stylus or microfluidic device to specific locations on the animal's body [9,14,15,37].
73 Although ideal for neuronal imaging, these techniques require the immobilization of animals with glue or
74 other techniques, and therefore, do not allow for reverse correlation analysis with behavior response
75 dynamics. Additionally, many of these techniques have a low experimental throughput, and cannot
76 provide the large sample sizes required for reverse correlation studies. One technique that overcomes
77 these challenges is to couple optogenetics with behavior, as a light stimulus is more easily controlled, and
78 can be used to activate specific neurons in freely moving animals [34,35,38]. This fictive stimulus has the added
79 benefit of bypassing differences in native receptor protein expressions, allowing for comparison between
80 sensory systems. In order to apply light stimuli with spatial resolution to activate specific regions of
81 sensory neurons, we adapted a previously developed tracking platform with selective illumination [39]. The
82 custom microscopy system uses a projector and computer vision tools to track the animal, allowing for
83 the delivery of spatially and temporally resolved stimuli required for white noise signal delivery.
84 Combining these tools, we developed an experimental and computational pipeline for performing
85 white noise analysis on *C. elegans*, and apply this method to elucidate models of transformations between
86 mechanosensory neuron activity and behavioral response. Using our platform, we computed linear filters
87 that characterize the dynamics of the gentle touch sensing TRNs and harsh touch sensing PVDs. These
88 filters provide a quantitative framework for the functions of these neurons, and allowed for the
89 investigation of differences in spatial encoding. Furthermore, this method allowed us to create models
90 that accurately predict behavioral changes in response to mechanosensory neuron activity. Our method
91 provides simple transformations that quantitatively characterize these systems by capturing the
92 spatiotemporal dynamics of behaviors induced by optogenetic activation of sensory neurons.
93

Results

Reverse-correlation analysis using optogenetics and behavior tracking

To illuminate the differences between the mechanosensory systems, we characterize and compare the dynamics for these two anatomically distinct sets of mechanosensory neurons: the gentle touch sensing TRNs and the harsh touch sensing PVDs (Fig 1A). In order to use reverse correlation for modeling behavioral responses, the two main experimental requirements are the delivery of a white noise stimulus and accurate measurements of the output. For the stimulus, we used optogenetics to directly activate the mechanosensory neurons with a white noise signal. This unmediated input enabled us to activate neurons regardless of expression of mechanotransductive channels. This allows the comparison of how the two systems and their morphologies control downstream activity, rather than differences in their sensory activation. Additionally, whereas a natural stimulus can activate additional sensory neurons and possibly interfere with the characterization, the optogenetic stimulus will only activate the neurons expressing channelrhodopsin. Therefore, the resulting filters characterize the dynamics of behaviors exclusively in response to activation of specific sensory neurons. Our tracking platform [39] enables the delivery of patterned illumination while simultaneously tracking individual animals, allowing for selective activation of specific sections of transgenic animals with high spatial and temporal precision (Fig 1B, Movie S1, Methods). We used this platform to deliver the white noise light stimulus for reverse correlation; we activate mechanosensory neurons with a pseudo-random m-sequence pattern, a spectrally unbiased binary signal (Methods).

The outputs we seek to characterize are the behavioral responses of animals using the optogenetic stimuli as inputs. We developed a custom computer vision algorithm (Methods) to analyze recordings of animals' behavior in a high-throughput and unbiased manner. The worm's posture and position are extracted for each frame, which are then used to quantify various "continuous" behaviors such as instantaneous velocity, instantaneous head angle, and instantaneous acceleration (Fig 1C). In

120 addition to these "continuous" behaviors we also quantified and categorized several classical "discrete"
121 behaviors such as reversals, pauses, and omega turns [18,40–42] (Fig 1C, Methods). Each of these continuous
122 and discrete variables was used as a separate output for reverse correlation analysis, yielding a filter that
123 can be used to predict behavior responses to any arbitrary stimulus patterns. By using filters for a large
124 portion of the worm's behavioral repertoire, we can describe the overall behavioral response when
125 stimulating specific mechanosensory neurons.

126 Using the white noise light stimulus for optogenetics and the quantified behavioral responses, we
127 next apply reverse correlation to model *C. elegans* response as transformations of linear and non-linear
128 filters. Classically, when characterizing mammalian neuronal systems, a neuron's response is modeled by
129 computing the average of the stimuli that preceded its action potentials (spike-triggered average or STA)
130 or its subthreshold voltages (voltage-weighted average or VWA) [29]. Analogously, we estimate the
131 dynamics of *C. elegans* response by computing the behavior weighted average of the stimulus (BWA).
132 When stimulating specific segments of the mechanosensory systems, the BWA represents how the
133 animals characteristically transform patterns of activity of those neurons into specific behaviors, providing
134 a filter estimation of this transformation (Fig 1D).

135 In order to accurately estimate these linear filters, a large sample size is required to test enough
136 input values [20,30]. To estimate the number of samples required in our system, we characterized the speed
137 of convergence of computed filters as the number of input samples increased (Movie S2). We
138 characterized the convergence of filters by computing the L2 norm of the difference between subsequent
139 filters (computed as the absolute difference between filters). We found that our system converges (to a
140 relative tolerance of $\delta<0.005$) after using roughly 30,000 frames of tracking data (Fig 1E). With our
141 experimental conditions, this is equivalent to a sample size of roughly 30 animals (Methods).

142

143 Linear Filters for anterior and posterior touch receptor neurons (TRNs) robustly capture behavioral

144 dynamics

145 We first used our method to characterize responses to the touch receptor neurons (TRNs:

146 ALML/R, AVM, PVM, and PLML/R) by using transgenic animals expressing channelrhodopsin (ChR2) under

147 the *mec-4* promotor (Methods)[39]. In response to natural stimuli, the posterior TRNs (PVM and PLML/R)

148 respond to posterior touch, inducing forward acceleration, whereas the anterior TRNs (ALML/R and AVM)

149 respond to anterior touch, inducing reversals [4,7,8,39,43]. To characterize the dynamics of these responses,

150 we applied an m-sequence light stimulus to either the anterior or posterior region of transgenic animals,

151 selectively stimulating the anterior or posterior TRNs, respectively (Fig 2A). We first computed linear filters

152 characterizing the relationship between anterior TRNs and either discrete or continuous behavior (Fig 2

153 and Fig S1). As a control, we also performed experiments with animals that were not fed all trans-retinol

154 (ATR), a cofactor required for ChR2 function. The computed filters for control animals are flat, zero-mean

155 signals (Fig 2, gray lines). In contrast, the acceleration BWA for the ATR-fed worms results in a filter with

156 a robust negative peak, -13 ± 0.50 $\mu m/s^2$ (Fig 2Ei). The presence of this peak in the experimental group

157 and its absence in the control group suggest that the filter is optogenetically induced, and not due to

158 spontaneous behavior. We attribute small fluctuations as experimental noise rather than representing a

159 true high frequency response. Lastly, this deceleration in the experimental group is expected from typical

160 reversal responses to anterior touch stimulation[4,7].

161 In order to further assess the validity of the resulting filters, we performed statistical tests

162 comparing true filters and filters computed from shuffled data (Methods). We compute magnitudes for

163 all filters, defined as the L2 norm, to the correctly computed filter. Data is shuffled in four different ways

164 (Methods). In all tests, the BWA computed from experimental data has the highest magnitude compared

165 to filters computed from shuffled data (Fig S2). Together with the statistical comparison of ATR-fed and

166 non ATR-fed animals, we conclude that the BWA for acceleration is robust and descriptive of the
167 behavioral response.

168 In addition, our method also reveals new information about the dynamics of these responses.
169 From the BWA, we can characterize metrics such as the delay to the peak (0.2s) and the decay timescale
170 of the filter (0.4s); these temporal characteristics are critical for accurately predicting response to
171 activation of the anterior TRNs. In comparison, the BWA computed with velocity also returns a linear filter
172 with a negative peak (-6.1 ± 0.39 μm/s), although with a longer delay to peak (0.7s) and longer decay
173 timescale (0.6s) (Fig S1). The difference between temporal characteristics of these two filters suggests
174 that although animals reverse for a relatively long time after the stimulus (1.3s), the deceleration portion
175 of this reversal only takes place in the first 0.6s after a stimulus.

176 To ensure that the computed linear filters are not an artifact from the input signal itself, we tested
177 computing filters using a different m-sequence stimulus. Using acceleration as an example, we observe a
178 similar linear filter to those obtained with the previous stimulus (Fig 2C, as compared to 2B). When
179 comparing the peak values of the filters computed with different stimuli, there is no statistical difference
180 (Fig 2Eii). These results demonstrate that the linear filters are indeed characteristic of *C. elegans*'
181 behavioral output specifically in response to the activity in the anterior TRNs, and independent of the
182 input signal.

183 Next, we sought to compare the dynamics of the animals' response between anterior or posterior
184 TRN activities. Previous findings have shown that applying a mechanical force to the posterior region of
185 the animal induces an acceleration, and PLM is required for these responses [4,7,8]. As with the anterior
186 TRNs, we stimulated the posterior TRNs by applying an m-sequence light stimulus to the posterior half of
187 the animal, and computed the BWA for the same quantified behaviors (Fig 2 and Fig S1). The filter for
188 acceleration has a positive peak (2.8 ± 0.48 $\mu m/s^2$), although with a much smaller magnitude than its
189 anterior counterpart and is not statistically significant compared to non ATR-fed worms (Fig 2D).

190 Additionally, the filter is not statistically significant when testing against filters for shuffled data (Fig S3).
191 Interestingly, although the computed linear filter for the posterior TRNs has a peak in the direction that is
192 consistent with previous findings, it is close to zero-mean. One interpretation that is consistent with
193 literature is that worms have a lower rate of responses when activating PLM and PVM in comparison to
194 the activating anterior TRNs. This is not surprising, as worms are generally moving forward and do not
195 require a change in behavior to escape the weak stimulus, whereas avoidance of a weak anterior stimulus
196 requires a directional change.

197 In addition to continuous signals, we also estimated linear filters for the probability of transitions
198 between defined states. Unlike in predicting continuous variables (e.g. acceleration and velocity), filters
199 computed for these behaviors indicate a change in probability of transitions to these behaviors. When
200 computing the BWA with transitions into pauses or reversals in response to anterior TRNs, we observe
201 linear filters with positive peaks that are statistically significant as compared to non ATR-fed animals (Fig
202 2F,G, I). Similarly, the filters computed from shuffled data support this statistical significance (Fig S3). This
203 indicates that activating the TRNs induce an increase in probability of transitions to pauses or reversals,
204 and this increased likelihood happens within the first second after a stimulus. In contrast, when
205 stimulating the posterior TRNs, the filter computed for transitions into pauses and reversals is close to
206 zero-mean, indicating that the stimulus does not alter these behaviors significantly (Fig 2H,I, and Fig S3).
207

208 Reverse Correlation Analysis of Harsh-Touch Sensing PVD Neurons

209 In addition to the TRNs, *C. elegans* has another set of neurons that are responsible for body touch
210 sensation. The PVD neurons are morphologically unique sensory neurons that have extensive and
211 organized dendritic structures expanding most of the body of the worm; in contrast, TRNs are tiled (Fig
212 1A). Additionally, the PVD neurons are known to respond to harsh touch, as opposed to gentle touch or
213 nose touch[5,10–13]. Because of the morphological and functional differences between the PVD and TRN

214 systems, we ask whether there are also downstream differences in spatial and temporal behavioral
215 response dynamics. To do so, we applied the same reverse correlation method to animals expressing ChR2
216 in the PVD neurons [13].

217 For comparison with the TRNs, we again divided the stimulus regions into anterior and posterior
218 segments, and computed the BWA and estimated linear filters for the same behaviors (Fig 3A).
219 Interestingly, when the animal is stimulated either anteriorly or posteriorly, the BWA's for acceleration
220 both have positive peaks (Fig 3B,C), indicating that activating either of these segments of PVD induces an
221 increase in velocity. This positive peak is also observed for both segments when computing the BWA with
222 velocity (Fig S4). However, only the filters from the posterior segment are statistically different from the
223 non-ATR group, with a higher positive peak for both acceleration (Anterior 4.0 ± 0.58 $\mu m/s^2$ vs Posterior
224 7.1 ± 0.58 $\mu m/s^2$) and velocity (Anterior 3.5 ± 0.32 µm/s vs Posterior 7.1 ± 0.32 µm/s) (Fig 3D and Fig S4).
225 When computing the BWA with transitions into pauses or reversals in response to either anterior or
226 posterior PVD, we observe flat, zero-mean linear filters (Fig 3 E, F). These filters are statistically
227 indistinguishable from the non-ATR fed control group (Fig 3G), indicating that activation of the PVDs do
228 not induce a change in probability of these events. When comparing these filters with shuffled data, only
229 the posterior acceleration filter is statistically significant (Fig S5). This contrast from the TRN filters
230 suggests a different role for PVD sensory neurons in the behavioral circuit – that PVD activation promotes
231 positive acceleration, and TRNs promote negative acceleration, consistent with previous findings [8,12].

232 In addition to the magnitudes, the context of peak occurrence can also be informative. The PVD
233 acceleration filters have significant negative peaks following the positive peaks; the magnitudes of the
234 negative peaks are of similar values to the first positive peak (Fig 3D). This suggests that the acceleration
235 in response to PVD activation is more likely to occur when preceded by a negative acceleration. In other
236 words, worms that are slowing down or reversing are more likely to respond to PVD activation and
237 produce a positive acceleration. In contrast, the anterior TRN acceleration filters only contain one

238 significant peak. These differences in the acceleration filters further supports the idea that PVD and TRNs
239 influence different aspects of behavior.
240

241 ## Linear-Nonlinear Models Predict Behavioral Response

242 In general, the filters computed from BWA in response to a white noise signal capture the linear
243 dynamics of the analyzed systems. However, biological systems are rarely linear[24]. A common approach
244 for modeling the nonlinear dynamics of a system is to use a linear-nonlinear cascade, where a static
245 nonlinear filter is used to characterize the nonlinear dynamics not captured by reverse correlation [20,23–25].
246 To define static nonlinear filters, we used the linear filters computed from BWA and compared predicted
247 outputs with measured experimental outputs (Methods). For instance, for acceleration in response to
248 anterior TRNs, we first compared predicted values with the quantified experimental values (Fig 4A, gray
249 circles). Not surprisingly, there is a positive correlation between predicted and experimental outputs,
250 indicating that the model does indeed capture linear dynamics in these responses. To capture the
251 nonlinear dynamics of the response, we fit a static filter using a simple quadratic function (Fig 4A blue
252 lines, Methods). Similarly, we also characterized nonlinear filters for velocity (Fig S6A) and transitions into
253 pauses or reversals (Fig 4B, Methods). The quadratic functions greatly improve the model fit to the data,
254 suggesting that they capture a large portion of the nonlinear dynamics of the anterior TRNs. We also
255 computed static nonlinear filters for stimulation of the posterior TRNs. In comparison to the anterior TRNs,
256 there is a lower correlation between experimental measurements and predicted values (Fig 4C,D, Fig S6B).
257 This is expected, as the estimated linear filters for these neurons were close to zero-mean, yielding a small
258 range of predicted responses. Furthermore, because the linear filters alone led to a low predictability of
259 responses for posterior TRNs, nonlinear functions also fail to capture a large portion of the variability in
260 responses (Fig 4C,D, Fig S6B, orange lines).

261 We next sought to test the validity of using linear-nonlinear (LN) cascade models to predict
262 behavioral responses to novel stimuli. To do this, we probed the anterior TRNs with a different m-
263 sequence stimulus from the one used to compute the filters (Fig 5A, Methods). We first compared the
264 measured velocities of animals to the predicted velocities when using the linear filter only (Fig 5B).
265 Although the magnitude of predicted velocity from the model did not exactly match the experimental
266 measurements, the model captures large features of the temporal dynamics of velocity in response to this
267 novel stimulus. Next, we incorporated the static nonlinear filter to predict velocities (Fig 5C). When using
268 the LN model, the magnitudes of predicted velocities are more similar to experimental values, leading to
269 more accurate predictions. In addition to predicting the continuous velocity of the animals, we also tested
270 L and LN models for pauses and reversals, and observe predicted increases in probability of events similar
271 to experimental values (Fig S7A,B). Incorporating the nonlinear component to these models also improves
272 the model predictability.

273 Interestingly, in our experiments we observe a time-dependent decrease in the magnitude of
274 responses, which fails to be captured in time-scales of the dynamic linear filters (Fig 5B,C latter half).
275 Biologically, this habituation of responses is commonly observed in sensory systems [44]. In general,
276 although LN models can predict system responses, this is true only to the time-scales captured in the
277 linear filters, and does not capture adaptation dynamics. To model this decay of responses, we add a
278 dynamic exponential function following the LN cascade (Fig 5A). We tested a wide range of decay rate
279 values using this model and found that a decay rate of 50s best provided the best predictions (Fig S8).
280 Interestingly, this decay rate is consistent with previous findings from investigations of habituation to
281 stimulation of TRNs, with both tapping and optogenetic stimuli [45]. When adding this exponential
282 component to our model, the accuracy of our model's predicted behavioral responses improves for later
283 time points of the trials, thus improving the overall accuracy of our models (Fig 5D, Fig S7C,D). These
284 results illustrate how the linear filters computed from BWA, when combined with additional nonlinear

285 filters, are powerful in predicting temporal dynamics of behavioral responses to sensory neuron
286 activation, and likely generalizable to other sensory responses.
287

288 Spatially Refined Selective Illumination Improves Resolution of Linear Filters from BWA

289 We have thus far characterized mechanosensory systems by probing either the anterior or
290 posterior segments of the animal, similar to previous investigations of the receptive fields of
291 mechanosensory systems [12,14]. To further examine the spatial resolution of the mechanosensory systems,
292 we took advantage of our selective-illumination light stimulus, which allows for the probing of specific
293 spatial segments as small as 14µm [39]. We characterized the TRN system with better resolution by
294 increasing the number of segments in our stimulus to 4 (Fig 6A). We applied an m-sequence stimulus
295 selectively to one of the four segments, and computed linear filters for both continuous and discrete
296 behavioral outputs (Fig 6 and Fig S9). This particular discretization of the TRN system allows for the
297 computation of separate filters for the processes and cell bodies of ALM and AVM, as well as separate
298 filters for PVM and PLM cell bodies (while keeping a high number of photons in the stimulus region). We
299 first computed filters for acceleration in response to stimulating four segments. The filters for the most
300 anterior quarter and second-most anterior quarter have a prominent negative peak, statistically
301 significant when compared to non-ATR fed animals (Fig 6B,C,F). These filters are also statistically
302 significant when compared to shuffled data (Fig S10). Interestingly, these filters are similar to the filter
303 computed from stimulating the entire anterior region (compare to Fig 2B,C). This suggests that there are
304 no observable differences in acceleration dynamics between cell body and axon activity of the anterior
305 TRNs.

306 Not surprisingly, the filters for acceleration in response to the most posterior quarter and second
307 most posterior quarter are both flat and are statistically indistinguishable from filters computed with non-
308 ATR fed animals (Fig 6D,E,F). These filters are also not statistically significant when comparing to shuffled

309 data (Fig S10). Similar to the anterior region, the acceleration filters for the separate posterior segments
310 are similar to the flat filter computed from stimulating the entire posterior region (compare to Fig 2D).
311 We next computed linear filters for transitions into pauses or reversals, and found differences in
312 spatial encoding. The results for the anterior segments did not reveal much spatial encoding, with the
313 filters for both the most anterior quarter and second-most anterior quarter both having positive peaks
314 (Fig 6G,H,K), similar to the filter computed when stimulating the entire anterior regions (compare to
315 Fig2F,H). These filters are also statistically significant when comparing to shuffled data (Fig S10). This
316 suggests that there is low spatial encoding of these discrete behavioral responses between the axons and
317 cell bodies of the anterior TRNs. Interestingly, we observe different filters when dividing the posterior
318 segment of the TRNs into separate segments for the cell bodies of PVM and PLM. The filter for the most
319 posterior quarter, which includes the PLM cell body, is again a flat filter (Fig 6J), similar to the filter
320 computed when stimulating the entire posterior region (compare to 2H). Surprisingly, the filter for
321 second-most posterior quarter has a negative peak, statistically significant when compared to non-ATR
322 fed animals (Fig 6I,K). This filter is also statistically significant when compared to shuffled data (Fig S10).
323 The negative peak indicates that there is a reduced probability of pauses and reversals when activating
324 PVM cell body. This suggests that PVM potentially has a previously undescribed function of inhibiting
325 pauses and reversals. Additionally, the difference in filters for the four segments implies that the TRNs
326 employ their tiled network to allow for spatial encoding of behavioral responses. This suggests that the
327 morphological differences between the tiled TRNs and branched PVDs are used to differently control
328 downstream activity.

329 Discussion

330 The nervous system continuously transduces sensory stimuli into neuronal activity and
331 appropriate behavioral outputs. One of the biggest challenges in mapping this neuronal encoding is the

332 lack of a quantitative framework for characterizing how a layer of neural activity is transduced into the
333 downstream circuit. In this work, inspired by previous work in modeling neuronal systems, we built a
334 framework that uses reverse correlation analysis with a custom tracking platform to analyze a *C. elegans*
335 sensory system. We investigated the spatial and temporal encoding of two mechanosensory systems, the
336 gentle touch sensing TRNs and the harsh touch sensing PVDs. We computed several linear filters that
337 quantitatively describe transformations between sensory neuron activity and behavioral outputs, and
338 support previous findings about the systems. Analysis of the PVDs produced linear filters that indicate an
339 increase in velocity and acceleration from their activation, which is consistent with literature on its
340 function [5,10–13]. Similarly, the linear filters computed for the TRNs were also consistent with previous
341 literature: the anterior TRNs show decreases in velocity and acceleration, and an increase in probability
342 of pauses and reversals [4,7,8,39,43], and the posterior TRNs show an increase in acceleration [4,8,39]. It should be
343 noted that we do not measure expression levels of ChR2 in the sensory systems, and any differences in
344 computed filters could be explained by differences in expression levels. However, when assuming uniform
345 expression levels across the sensory systems, our results provide spatiotemporal receptive fields for these
346 systems that are consistent with previous findings [7].

347 The linear filters resulting from our method provide several insights into the circuitry and
348 morphological differences between the two sensory systems. First, although we used identical stimuli for
349 both segments, the filters produced from activating the anterior TRNs were much more robust than the
350 filters from activating the posterior TRNs, suggesting that downstream interneurons in this circuit are
351 more responsive to the anterior neurons. This preference in downstream activity has also been observed
352 in experiments involving tap responses, which show that reversals dominate over accelerations when
353 tapping cultured plates, and this preference occurs downstream of sensory neuron activity [8]. In contrast,
354 the filters for the posterior segments of PVD were more robust than the anterior segments. This is also
355 consistent with previous findings that show PVD is required for posterior harsh touch sensation, but not

356 required for anterior harsh touch [12]. A key difference in our experiments is that we bypass
357 mechanoreceptor activation, and can therefore separate out effects due to differences in sensory neuron
358 response to different spatial stimuli, as well as other neurons that might affect response rate. Therefore,
359 one possible mechanism for the differential decision-making is that the two mechanosensory systems
360 may have different strengths of connections to postsynaptic command interneurons. Particularly for PVD,
361 although the number of physical synapses to forward command neuron PVC and backward command
362 neuron AVA are similar [46], the functional connectivity seems to be higher for PVC compared to AVA. Our
363 results strongly support this hypothesis.

364 Our results also provide insight on the levels of spatial encoding in the TRNs and PVD systems.
365 The TRNs, which employ a tiled network to cover the body, appear to have more spatial encoding. When
366 comparing the computed filters for the anterior and posterior TRNs, most behaviors show distinct
367 differences in responses. Furthermore, when analyzing this system in four segments, we observed
368 differences in linear filters among the four segments. In contrast, the branched network in PVD does not
369 appear to spatially encode behavioral responses. The filters from activating the anterior and posterior
370 segments of the PVD system have similar dynamics, with the anterior filters having slightly smaller
371 magnitudes and longer delays. This contrast between the two mechanosensory systems suggests that
372 although both the TRNs and PVDs have spatially distributed processes to sense touch throughout the
373 body, the unique morphological strategies in the two systems lead to differences in their capabilities of
374 encoding responses. Biologically, this disparity in encoding can be explained by their morphologies and
375 perhaps synaptic connectivity to downstream neurons, as the tiled TRN system consists of more nodes,
376 which could allow for more spatially specific behavioral responses.

377 One new finding from our experiments concerns the role of the cryptic PVM neuron. Although
378 shown to respond to mechanical stimuli [47], its role in mediating behavior is poorly understood [4,7,8,39]. We
379 found that activating PVM did not induce significant changes in velocity, but induced a slight decrease in

380 acceleration. Interestingly, PVM activation significantly reduced the probability of reversal events. These
381 filters suggest a unique function for PVM in modulating escape response. In contrast to the other TRNs,
382 PVM does not induce escape responses, but rather suppresses these behaviors, as well as decrease the
383 velocity of forward movement.

384 The findings in this work demonstrate the utility of our method for providing new insights into
385 the dynamics of the mechanosensory system in *C. elegans*, one of the earliest and better characterized
386 neural circuits. By using a quantitative framework to compare the dynamics between the two sensory
387 systems, we recapitulated qualitative findings from previous literature, and provide further insights in the
388 temporal and spatial encoding in these systems. Additionally, we used linear filters computed from BWA
389 to create LNE models that can predict the behavioral responses of animals in response to activity in
390 sensory neurons alone. Because this method is noninvasive and independent of natural stimulus, it can
391 be easily extended to investigate the dynamics of other neural circuits in *C. elegans* and other model
392 organisms. We foresee many potential applications in better understanding sensory behavior responses
393 and sensory integration.

394

395 Methods and Materials

396 *C. elegans* Culture and Maintenance. We used transgenic worms expressing channelrhodopsin in
397 various mechanosensory neurons. Worm populations were cultured at 20C in the dark on standard
398 nematode growth medium (NGM) petri dishes. Plates were coated with OP50 bacteria lawn
399 supplemented with the cofactor required for channelrhodopsin, all-*trans*-retinal (Sigma-Aldrich). The
400 solution was prepared by diluting a 50mM stock solution (in ethanol) in OP50 suspension to a final
401 concentration of 100uM. Control animals were grown in parallel on OP50 without all-*trans*-retinal. All
402 worms tested were F1 progeny of P0 adults picked onto seeded plates 3-4 days before experiments.

403 Animals were washed to unseeded NGM plates 1hr prior to assays. Animals were then picked to individual
404 plates for experiments. Each animal was exposed to a single stimulus profile and then discarded. The
405 strains used in this work included AQ2334: *lite-1(ce314); ljIs123[pmec-4::ChR2; punc-122::rfp*] [39] and
406 ZX899: *lite-1(ce314); ljIs123[pmec-4::ChR2; punc-122::rfp*] [13].
407
408 Tracking and Light Delivery Platform. Experiments were performed on a tracking system adapted from
409 a previously developed projector based microscopy system [39]. The system uses an inverted microscope
410 (Leica-DMIRB) with a low-magnification objective (x4) to image freely moving animals. We image using
411 near-infrared light by applying a long-pass filter (715nm) to the transmitted light path and capture images
412 using a large sensor NIR camera (Basler acA2040-180kmNIR), which limits interference in blue light used
413 for optogenetics stimulus. A three-color LCD projector is used as the light source for optogenetic stimulus
414 with selective illumination. We use a camera with large sensor area to capture the full body of the animal,
415 and use a small ROI and binning to reduce the size of images to improve processing speed and therefore
416 tracking rate. A Lenovo desktop computer with an Intel Core i74790 Processor (8MB Cache, up to 4.0GHz)
417 and a 512GB Solid State Drive and 16GB RAM was used to process images for tracking and selective
418 illumination. Tracking of individual animals was performed by using images taken with the camera, and
419 processed to compute the centroid of the animal in terms of x-y pixels on the camera FOV. Based on the
420 position of the computed centroid, a command is sent to a motorized stage to move the animal to the
421 center of the FOV. To apply a light stimulus with spatial and temporal control, we used a modified
422 projector as the light source to the microscope. Images taken with the camera are processed to determine
423 the outline of the animal's body in each frame. The appropriate illumination pattern is then computed
424 and sent to the projector. Stimuli were only presented when ansterior and posterior segments were
425 correctly computed by the algorithm; during pirouettes or other uncommon postures, stimulus

426 presentation was paused. This process was performed at a rate of 13 frames per second. For each animal,
427 illumination profile and tracking videos were saved for future analysis.
428
429 Quantitative Behavior Analysis. To extract quantitative behavioral features from tracking recordings, a
430 custom MATLAB script was developed. A series of segmentation and morphological processes were used
431 to extract body postures in each frame. We combined extracted postures with recorded stage movements
432 to quantify several behaviors. We computed various "continuous" behaviors that have a scalar value for
433 each time point. This includes velocity (magnitude), velocity (angle), acceleration, head angle, angular
434 velocity. We also classified various "discrete" behaviors that have been used in previous works [18,40,48,49].
435 These include behaviors such as pauses, reversals, omega turns, and turns. Each of these behaviors were
436 classified by applying thresholds on quantified continuous behaviors. Pauses and reversals were classified
437 by applying both vertical and horizontal thresholds on velocity measurements. Omega turns were
438 classified by applying a threshold on the eccentricity of the animal's posture. Curves were classified by
439 applying a threshold on the angle of position trajectory.
440
441 White Noise Experiments. We used the selective illumination capability of the tracking system to deliver
442 spatially controlled light stimuli to freely moving animals expressing ChR2 in their mechanosensory
443 neurons. We used a pseudorandom m-sequence, a binary signal with unbiased spectrum, with similar
444 properties to a Gaussian white noise signal [22,31]. We tested several white noise signals, and found that an
445 m-sequence with a maximum frequency of 2Hz produced reliable results, as it allows for testing time
446 scales appropriate for behavioral responses. We use a light intensity of $0.75 mW/mm^2$ as it induces reliable
447 and varying behavioral responses, similar to previous work [39]. The generated pseudorandom sequences
448 were repeats of a 6-bit words, 63 value length m-sequences ($2*(2^6-1) = 126$ values). We deliver the same
449 pseudorandom signal for each experimental group, applying the signal through the tracking system and

450 changing values in the m-sequence at 2Hz, which is lower than the Nyquist Frequency (acquisition rate is
451 13Hz). Stimuli were only presented when ansterior and posterior segments were correctly computed by
452 the tracking algorithm; during pirouettes or other uncommon postures, stimulus presentation was
453 paused.
454
455 Reverse Correlation Analysis. To compute mathematical functions that describe the transformations
456 from sensory neuronal activity into behavior, we first modeled the entire animal as a linear transducer:

457 $$o(t) = h(t) * s(t) = \int_{-\infty}^{\infty} h(\tau)s(t-\tau)d\tau \qquad (1)$$

458 where the relationship between the input signal (neuronal activity through optogenetics) s(t) and output
459 signal (behavior) o(t) is characterized by a function h(t). We assume that the system is causal, and h(t)<0
460 for t<0. We used standard reverse-correlation similar to [29–31,34,35], and computed h(t) for specific behaviors
461 by computing a "behavior-weighted-average" (BWA):

462 $$h(t) \sim BWA = \frac{1}{N}\sum_{\tau} \overrightarrow{s_{\tau-t}} \times v_o(\tau) \qquad (2)$$

463 where the stimulus preceding each time-point is weighed by the scalar value of the behavior at that time.
464 We convert the light stimulus patterns into -1 and 1 for when the light is on and off, respectively. For
465 continuous behaviors, we used the scalar values at each time points as the weights. For discrete behaviors,
466 we used a binary signal indicating transitions from forward movement to specific states. For all cases, we
467 compute linear filters using 400 points preceding and following each time point (801 total timepoints).
468 The points preceding each time point are computed as a control to capture experimental variablity.
469
470 Statistical Significance of Computed Filters. Behavior-weighted averages (BWAs) were tested for
471 significance by comparing their magnitude, computed as the L2 norm, to a distribution of random filters
472 computed with shuffled data. We tested four different methods of shuffling data: cyclic shuffling of the

stimulus vector by a random integer, cyclic shuffling of the output vector by a random integer, random permutations of the stimulus vector, and random permutations of the output vector. For each test, we perform the same computation with the shuffled data and repeat 100 times. The BWA is classified as significant if its magnitude is higher than all shuffled data tests. Random integers were generated from a uniform distribution from 1 to length of vector using the MATLAB function rand, and random permutations of vectors were performed using the MATLAB function randperm.

Nonlinear Filters and Model Predictions. We model static nonlinear filters for each behavioral response in order to extract the nonlinear dynamics not captured in the linear filters computed from reverse correlation [50]. We first compute linear model predictions by convolving the computed linear filters from presented stimuli in each trial used, as shown in equation (1). We then compare these linear predictions to the measured outputs at each time point, and fit a quadratic function. For "discrete" behaviors, probabilities for transitions into specific behaviors were calculated at each time point. These quadratic functions are then used as static nonlinear filters in a linear-nonlinear (LN) cascade model for specific behavior transformations.

$$y_{pN}(\mathrm{t}) = F_N(y_{pL}) \qquad (3)$$

where the predicted nonlinear output is a static function of the predicted linear output. We also apply an exponential decay filter (LNE) to capture nonlinear adaptations to the stimuli. We apply this exponential factor to only the changes in behavior after the stimulus:

$$y_{pE}(t > 5) = (y_{pN}(t > 5) - \mathrm{avg}(y_{pN}(t < 5)) * \exp(-\lambda t) + \mathrm{avg}(y_{pN}(t < 5)) \quad (4)$$

where the decay parameter λ is 50s, based on empirical data (Fig S8) and previous findings[45]. We use bootstrap sampling to compute 95% confidence intervals for our model predictions. Confidence intervals were computed using the MATLAB functions bootstrp and bootci, computed with 1000 resamples of the stimulus data.

Statistics. Linear filters are presented as mean ± SEM as computed by the BWA. The two-tailed Student's t-test was used to compare filter peaks between two groups. Peaks were determined by searching for local maxima in the filters between $-1 < t < 1$. $P<0.005$ was considered statistically significant. Accuracy of best-fit nonlinear filters were computed as coefficients of determination (R^2 values). Performance of models were compared using the sum of squared error (SSE). Values are normalized to the SSE value for linear models.

Code Availability. All custom code used to generate results in this manuscript are available on Github (https://github.gatech.edu/pages/dporto3/BWA-v1/).

Data Availability. All behavior and stimulus data generated during the current study are available from the corresponding author upon reasonable request.

Acknowledgments

The authors gratefully acknowledge the funding support of the US National Institutes of Health (R01NS096581, R01GM088333, R21EB021676, and R21EB020424 to HL).

Author Contributions

DP and HL designed experiments. DP, JG, and YZ performed experiments. DP wrote the manuscript and prepared all figures. All authors reviewed the manuscript.

Competing Interests

The authors declare no competing interests.

References

1. Kandel, E. R., Schwartz, J. H., Jessell, T. M., Siegelbaum, S. A. & Hudspeth, A. J. *Principles of Neural Science, Fifth Edition*. *Neurology* **3,** (2014).

2. White, J. G., Southgate, E., Thomson, J. N. & Brenner, S. THE STRUCTURE OF THE NERVOUS-SYSTEM OF THE NEMATODE CAENORHABDITIS-ELEGANS. *Philos. Trans. R. Soc. London Ser. B-Biological Sci.* **314,** 1–340 (1986).

3. Sengupta, P. & Samuel, A. D. T. Caenorhabditis elegans: a model system for systems neuroscience. *Curr. Opin. Neurobiol.* **19,** 637–643 (2009).

4. Chalfie, M. *et al.* THE NEURAL CIRCUIT FOR TOUCH SENSITIVITY IN CAENORHABDITIS-ELEGANS. *J. Neurosci.* **5,** 956–964 (1985).

5. Chalfie, M. & Au, M. Genetic control of differentiation of the Caenorhabditis elegans touch receptor neurons. *Science (80-.).* **243,** (1989).

6. Wicks, S. R. & Rankin, C. H. Integration of mechanosensory stimuli in Caenorhabditis elegans. *J. Neurosci.* **15,** 2434–44 (1995).

7. Goodman, M. B. Mechanosensation. *WormBook* 1–14 (2006).

8. Wicks, S. R., Roehrig, C. J. & Rankin, C. H. A Dynamic Network Simulation of the Nematode Tap Withdrawal Circuit: Predictions Concerning Synaptic Function Using Behavioral Criteria. *J. Neurosci.* **16,** (1996).

9. Suzuki, H. *et al.* In vivo imaging of C-elegans mechanosensory neurons demonstrates a specific role for the MEC-4 channel in the process of gentle touch sensation. *Neuron* **39,** 1005–1017 (2003).

10. Albeg, A. *et al.* C-elegans multi-dendritic sensory neurons: Morphology and function. *Mol. Cell. Neurosci.* **46,** 308–317 (2011).

11. Chatzigeorgiou, M. *et al.* Specific roles for DEG/ENaC and TRP channels in touch and thermosensation in C. elegans nociceptors. *Nat. Neurosci.* **13,** 861-U106 (2010).

12. Li, W., Kang, L., Piggott, B. J., Feng, Z. & Xu, X. Z. S. The neural circuits and sensory channels mediating harsh touch sensation in Caenorhabditis elegans. *Nat. Commun.* **2,** (2011).

13. Husson, S. J. *et al.* Optogenetic Analysis of a Nociceptor Neuron and Network Reveals Ion Channels Acting Downstream of Primary Sensors. *Curr. Biol.* **22,** 743–752 (2012).

14. Nekimken, A. L. *et al.* Pneumatic stimulation of C. elegans mechanoreceptor neurons in a microfluidic trap. *Lab Chip* (2017). doi:10.1039/C6LC01165A

15. Cho, Y. *et al.* Automated and controlled mechanical stimulation and functional imaging in vivo in C. elegans. *Lab Chip* **17,** 2609–2618 (2017).

16. Stephens, G. J., de Mesquita, M. B., Ryu, W. S. & Bialek, W. Emergence of long timescales and stereotyped behaviors in Caenorhabditis elegans. *Proc. Natl. Acad. Sci. U. S. A.* **108,** 7286–7289

(2011).

17. Brown, A. E. X., Yemini, E. I., Grundy, L. J., Jucikas, T. & Schafer, W. R. A dictionary of behavioral motifs reveals clusters of genes affecting Caenorhabditis elegans locomotion. *Proc. Natl. Acad. Sci. U. S. A.* **110,** 791–796 (2013).

18. Yemini, E., Jucikas, T., Grundy, L. J., Brown, A. E. X. & Schafer, W. R. A database of Caenorhabditis elegans behavioral phenotypes. *Nat. Methods* **10,** 877–+ (2013).

19. Abbott, P. D. and L. F. in (The MIT Press, 2001).

20. Simoncelli, E. P., Paninski, L., Pillow, J. & Schwartz, O. *Characterization of Neural Responses with Stochastic Stimuli*. *Cognitive Neurosciences Iii, Third Edition* (2004).

21. Chichilnisky, E. J. A simple white noise analysis of neuronal light responses. *Network-Computation Neural Syst.* **12,** 199–213 (2001).

22. Ringach, D. & Shapley, R. Reverse correlation in neurophysiology. *Cogn. Sci.* **28,** 147–166 (2004).

23. Sharpee, T. O. Computational Identification of Receptive Fields. *Annu. Rev. Neurosci. Vol 36* **36,** 103–120 (2013).

24. Nykamp Siam J Appl Math, D. Q. WHITE NOISE ANALYSIS OF COUPLED LINEAR-NONLINEAR SYSTEMS *. *Soc. Indiustrial Appl. Math.* **63,** 1208–1230 (2003).

25. Hunter, I. W. & Korenberg, M. J. The identification of nonlinear biological systems: Wiener and Hammerstein cascade models. *Biol. Cybern.* **55,** 135–144 (1986).

26. Sakai, H. M. WHITE-NOISE ANALYSIS IN NEUROPHYSIOLOGY. *Physiol. Rev.* **72,** 491–505 (1992).

27. Bredfeldt, C. E. & Ringach, D. L. Dynamics of spatial frequency tuning in macaque V1. *J. Neurosci.* **22,** 1976–1984 (2002).

28. DeAngelis, G. C., Ohzawa, I. & Freeman, R. D. Receptive-field dynamics in the central visual pathways. *Trends Neurosci.* **18,** 451–458 (1995).

29. Ramirez, A. *et al.* Spatiotemporal receptive fields of barrel cortex revealed by reverse correlation of synaptic input. *Nat. Neurosci.* **17,** 866–875 (2014).

30. Behnia, R., Clark, D. A., Carter, A. G., Clandinin, T. R. & Desplan, C. Processing properties of ON and OFF pathways for Drosophila motion detection. *Nature* **512,** 427–430 (2014).

31. Kato, S., Xu, Y., Cho, C. E., Abbott, L. F. & Bargmann, C. I. Temporal Responses of C. elegans Chemosensory Neurons Are Preserved in Behavioral Dynamics. *Neuron* **81,** 616–628 (2014).

32. Coen, P., Clemens, J. & Weinstein, A. Dynamic sensory cues shape song structure in Drosophila. *Nature* **507,** 233–7 (2014).

33. Clemens, J. *et al.* Connecting Neural Codes with Behavior in the Auditory System of Drosophila. *Neuron* **87,** 1332–1343 (2015).

34. Hernandez-Nunez, L. *et al.* Reverse-correlation analysis of navigation dynamics in Drosophila larva using optogenetics. *Elife* **4,** e06225 (2015).

35. Gepner, R., Mihovilovic Skanata, M., Bernat, N. M., Kaplow, M. & Gershow, M. Computations

underlying Drosophila photo-taxis, odor-taxis, and multi-sensory integration. *Elife* **4,** e06229 (2015).

36. Liu, M., Sharma, A. K., Shaevitz, J. W. & Leifer, A. M. Temporal processing and context dependency in Caenorhabditis elegans response to mechanosensation. *Elife* **7,** (2018).

37. Eastwood, A. L. *et al.* Tissue mechanics govern the rapidly adapting and symmetrical response to touch. *Proc. Natl. Acad. Sci. U. S. A.* **112,** E6955-63 (2015).

38. Shipley, F. B., Clark, C. M., Alkema, M. J. & Leifer, A. M. Simultaneous optogenetic manipulation and calcium imaging in freely moving C-elegans. *Front. Neural Circuits* **8,** (2014).

39. Stirman, J. N. *et al.* Real-time multimodal optical control of neurons and muscles in freely behaving Caenorhabditis elegans. *Nat. Methods* **8,** 153-U78 (2011).

40. Gray, J. M., Hill, J. J. & Bargmann, C. I. A circuit for navigation in Caenorhabditis elegans. *Proc. Natl. Acad. Sci. U. S. A.* **102,** 3184–3191 (2005).

41. Geng, W., Cosman, P., Berry, C. C., Feng, Z. & Schafer, W. R. Automatic tracking, feature extraction and classification of C elegans phenotypes. *IEEE Trans. Biomed. Eng.* **51,** 1811–1820 (2004).

42. Albrecht, D. R. & Bargmann, C. I. High-content behavioral analysis of Caenorhabditis elegans in precise spatiotemporal chemical environments. *Nat. Methods* **8,** 599-U120 (2011).

43. Leifer, A. M., Fang-Yen, C., Gershow, M., Alkema, M. J. & Samuel, A. D. T. Optogenetic manipulation of neural activity in freely moving Caenorhabditis elegans. *Nat. Methods* **8,** 147-U71 (2011).

44. Rose, J. K. & Rankin, C. H. Analyses of habituation in Caenorhabditis elegans. *Learn. Mem.* **8,** 63–69 (2001).

45. Timbers, T. A., Giles, A. C., Ardiel, E. L., Kerr, R. A. & Rankin, C. H. Intensity discrimination deficits cause habituation changes in middle-aged Caenorhabditis elegans. *Neurobiol. Aging* **34,** 621–631 (2013).

46. Altun, Z.F., Herndon, L.A., Wolkow, C.A., Crocker, C., Lints, R. and Hall, D. . WormAtlas. at <http://www.wormatlas.org>

47. Cho, Y. *et al.* High-Throughput Controlled Mechanical Stimulation and Functional Imaging In Vivo. *bioRxiv* (2017). doi:https://doi.org/10.1101/107318

48. Huang, K.-M., Cosman, P. & Schafer, W. R. Automated detection and analysis of foraging behavior in Caenorhabditis elegans. *J. Neurosci. Methods* **171,** 153–164 (2008).

49. Larsch, J., Ventimiglia, D., Bargmann, C. I. & Albrecht, D. R. High-throughput imaging of neuronal activity in Caenorhabditis elegans. *Proc. Natl. Acad. Sci. U. S. A.* **110,** E4266-73 (2013).

50. Korenberg, M. J. & Hunter, I. W. THE IDENTIFICATION OF NONLINEAR BIOLOGICAL-SYSTEMS - LNL CASCADE MODELS. *Biol. Cybern.* **55,** 125–134 (1986).

Figure Legends

Fig 1: Reverse correlation analysis of mechanosensory neurons enabled by tracking and selective illumination platform.

(A) Mechanosensory neurons characterized in this study. The gentle touch sensing neurons ALML/R, AVM, PVM, and PLML/R (blue) and harsh touch sensing neurons PVDL/R (red). (B) Schematic of custom tracking system with selective illumination used for reverse correlation experiments (Methods). A projector is used as the light source to enable selective illumination. Captured video frames are processed in real-time to deliver accurate light patterns on moving animals. (C) Sample stimulus and extracted quantified behavior traces obtained from the custom platform and analysis script (Methods). Input is a binary signal of On and Off. Outputs are characterized for both “discrete” and “continuous” behaviors. Discretized behaviors are classified based on a custom behavior analysis script (Methods). Colors represented in sample output: dark blue represents a pause, red represent reversals, light blue represents turns. (D) A sample filter computed using the BWA computation (Acceleration Response to Anterior TRN, n = 88,031 time-points). (E) The speed of convergence for the BWA as a function of the amount of data used to train the model. The error converges to a relative tolerance of $\delta<0.005$ after 30,000 time-points.

Fig 2: Linear filters for the touch receptor neurons (TRNs) responses are robust and reproducible.

(A) Stimulus patterns and neurons being analyzed. Animals used in these experiments express channelrhodopsin using the mec-4 promoter (Methods). (B-D) Linear filters computed from BWA for acceleration when stimulating the anterior (B,C) or posterior (D) TRNs. (E) Comparisons of peak values from computed linear filters in B-D. (F-H) Linear filters computed from BWA for pauses and reversals when stimulating the anterior (F,G) and the posterior (H) TRNs with an m-sequence. (I) Comparisons of

peak values from computed linear filters in F-H. Colored plots represent filters computed from ATR-fed animals, black plots represent filters computed from control (not ATR-fed) animals. Dark line and light shade represent BWA and SEM, respectively (sample sizes listed in Table S1). Error bars in bar plots indicate SEM (sample sizes listed in Table S1). Statistical significance for peaks computed using student's t-test (***p<0.001) and statistical significance of filters computed using shuffled data (Fig S2).

Fig 3: Linear filters for PVD activity illuminate dynamic differences between gentle and harsh touch systems.

(A) Stimulus patterns and PVD neurons being analyzed. (B,C) Linear filters computed from BWA for acceleration when stimulating the anterior (B) or posterior (C) regions of PVD. (D) Comparisons of peak values from computed filters. (E,F) Linear filters computed for pauses and reversals when stimulating the anterior (E) and posterior (F) regions. (G) Comparisons of peak values from computed filters. Colored plots represent filters computed from ATR-fed animals, black plots represent filters computed from control (not ATR-fed) animals. Dark line and light shade represent BWA and SEM, respectively (sample sizes listed in Table S1). Error bars in bar plots indicate SEM (sample sizes listed in Table S1). Statistical significance for peaks computed using student's t-test (***p<0.001) and statistical significance of filters computed using shuffled data (Fig S4).

Fig 4: Static nonlinear filters capture nonlinear dynamics in behavioral outputs. Estimation of static filters to capture nonlinear dynamics. (A,B) Static nonlinear filters fitted using predicted values from the linear filter (x-axis) and experimental values (y-axis) when stimulating the anterior TRNs, for (A) acceleration and (B) transitions into pauses and reversals. (C,D) Static nonlinear filters when stimulating the posterior TRNs, for (C) acceleration and (D) transitions into pauses and reversals. Linear filters and experimental values are subsets of data used in Figure 2 (n=600 for all conditions). Colored traces

677 represent computed nonlinear filters and gray dots represent independent time-points from measured
678 and predicted values. Probability of discrete events is computed as the probability of an event occurring
679 at a given time point.
680

681 Fig 5: Linear-Nonlinear-Exponential (LNE) model accurately predicts behavioral response.

682 (A) Block diagram of LNE model for used to predict behavioral responses to mechanosensory neuron
683 activity: a LTI system modeled from BWA, followed by a static nonlinear filter and exponential decay
684 filter. (B-D) Predictions of velocity for L (B), LN (C), and LNE (D) models (blue) and experimental traces
685 (black). For experimental data, dark line and shade represent average and SEM, respectively (n = 31
686 animals). For model predictions, dark line represents model prediction and shaded area represents the
687 95% confidence interval (Methods). (E) Comparison of performance of models, computed as the sum of
688 squared error (SSE) and normalized to the linear model performance value (Methods).
689

690 Fig 6: Decreasing the size of stimulus region allows for the estimation of a spatiotemporal
691 receptive field with higher resolution.

692 (A) Stimulus patterns used to analyze TRNs with improved spatial resolution. (B-E) Linear filters
693 computed for acceleration when stimulating the most anterior (B), the second-most anterior quarter (C),
694 second-most posterior quarter (D), and the most posterior quarter (E) of the TRNs with an m-sequence.
695 (F) Comparisons of peak values from computed filters in B-E. Error bars indicate SEM (sample sizes listed
696 in Table S1). (G-J) Linear filters computed for acceleration when stimulating the most anterior (G), the
697 second-most anterior quarter (H), second-most posterior quarter (I), and the most posterior quarter (J)
698 of the TRNs with an m-sequence. Colored plots represent filters computed from ATR-fed animals, black
699 plots represent filters computed from control (not ATR-fed) animals. Dark line and light shade represent
700 BWA and SEM, respectively (sample sizes listed in Table S1). (K) Comparisons of peak values from

computed filters in B-E. Error bars indicate Standard deviation. Statistical significance for peaks computed using student's t-test (***p<0.001) and statistical significance of filters computed using shuffled data (Fig S10).

Supplementary Information Legends

Movie S1: Example trial of white noise stimulation in our platform. An m-sequence light signal is delivered to either the anterior or posterior segment of the animal while simultaneously being tracked. For each trial, various discrete and continuous behaviors are quantified (Methods).

Movie S2: Sample filter computed using BWA as a function of sample size used for the computation.

Figure S1: Additional linear filters for TRNs. Linear filters computed for various behaviors when stimulating the anterior TRNs with an m-sequence signal (left), a different m-sequence signal (center), and the posterior TRNs (right). Dark line and light shade represent BWA and SEM, respectively. Colored plots represent filters computed from ATR-fed animals, black plots represent filters computed from control (not ATR-fed) animals. Sample sizes listed in Table S1.

Figure S2: Comparison of shuffled data significance tests. Results from comparison of four methods of shuffling data for statistical significance tests of linear filters. (A) Cyclic shuffling of stimulus vector by a random integer. (B) Cyclic shuffling of behavior vector by a random integer. (C) Random permutation of stimulus vector. (D) Random permutation of behavior vector. Bar plots represent the magnitude of filters, computed as the L2 norm, and are plotted in ranked order from highest to lowest magnitude.

725 Colored bar represents appropriately computed filter, gray bars represent filters computers with
726 shuffled data.
727
728 Figure S3: Significance test results for linear filters for TRNs. Results from shuffled data significance
729 tests for linear filters computed for activation of TRNs in Figure 2. (A-C) Significance test results for
730 computed filters for acceleration for anterior TRNs (A,B) and posterior TRNs (C). (D-F) Significance test
731 results for computed filters for pauses and reversals for anterior TRNs (D,E) and posterior TRNs (F). Bar
732 plots represent the magnitude of filters, computed as the L2 norm, and are plotted in ranked order from
733 highest to lowest magnitude. Colored bar represents appropriately computed filter, gray bars represent
734 filters computers with shuffled data.
735
736 Figure S4: Additional linear filters for PVDs. Linear filters computed for various behaviors when
737 stimulating the anterior (left) and posterior (right) PVDs with an m-sequence signal. Dark line and light
738 shade represent BWA and SEM, respectively. Colored plots represent filters computed from ATR-fed
739 animals, black plots represent filters computed from control (not ATR-fed) animals. Sample sizes are
740 listed Table S1.
741
742 Figure S5: Significance test results for linear filters for PVD. Results from shuffled data significance
743 tests for linear filters computed for activation of PVD in Figure 3. (A,B) Significance test results for
744 computed filters for acceleration for anterior (A) and posterior (B) segments of PVD. (C,D) Significance
745 test results for computed filters for pauses and reversals for anterior (C) and posterior (D) segments of
746 PVD. Bar plots represent the magnitude of filters, computed as the L2 norm, and are plotted in ranked
747 order from highest to lowest magnitude. Colored bar represents appropriately computed filter, gray
748 bars represent filters computers with shuffled data.

749

750 Figure S6: Static nonlinear filters for velocity. Static nonlinear filters fitted for predicted values from
751 the linear filter (x-axis) against experimental values (y-axis) when stimulating the anterior TRNs. Linear
752 filters and experimental values are subsets of data used in Figure 2 (n>1,730 for all conditions). Colored
753 traces represent computed nonlinear filters and gray dots represent independent time-points from
754 measured and predicted values.

755

756 Figure S7: Model predictions of reversal initiations. Comparison of model predictions of reversal
757 transitions (blue) and experimental traces (black) when using A) only the linear filter, B) a linear-
758 nonlinear (LN) model, and C) an additional exponential component (LNE). For experimental data, dark
759 line and shade represent average and SEM, respectively (n = 31 animals). For model predictions, dark
760 line represents model prediction and shaded area represents the 95% confidence interval (Methods).
761 Probability of reversal transitions is computed as the average of animals initiating a reversal at that time
762 point. D) Comparison of performance of models, computed as the sum of squared error (SSE) and
763 normalized to the linear model performance value.

764

765 Figure S8: Comparison of decay factors. Comparison of model predictions of velocity for various
766 exponential decay factors. Exponential decays of 2.5s, 5s, 50s, and 100s were tested, with 50s showing
767 the best fit. Performance of models is computed as the sum of squared error (SSE), normalized to the
768 linear model performance value.

769

770 Figure S9: Additional filters for spatially refined analysis of TRNs Linear filters computed for various
771 behaviors when stimulating the most anterior quarter (left), the second-most anterior quarter (second
772 from left), the second-most posterior quarter (second from right), and the most posterior quarter (right)

773 of the TRNs with an m-sequence signal. Dark line and light shade represent BWA and SEM, respectively.
774 Colored plots represent filters computed from ATR-fed animals, black plots represent filters computed
775 from control (not ATR-fed) animals. Sample Sizes are listed Table S1.
776
777 Figure S10: Significance test results for linear filters for refined TRN analysis. Results from shuffled
778 data significance tests for linear filters computed for activation of TRNs in Figure 6. (A-D) Significance
779 test results for computed filters for acceleration for most anterior (A), second-most anterior (B), second-
780 most posterior (C), and most posterior (D) segments of TRNs. (E-H) Significance test results for
781 computed filters for pauses and reversals for most anterior (E), second-most anterior (F), second-most
782 posterior (G), and most posterior (H) segments of TRNs. Bar plots represent the magnitude of filters,
783 computed as the L2 norm, and are plotted in ranked order from highest to lowest magnitude. Colored
784 bar represents appropriately computed filter, gray bars represent filters computers with shuffled data.
785
786 Table S1: Sample sizes for computed linear filters in figures 2, 3, 4, 6, S1, S2, and S9.
787

Figure 1

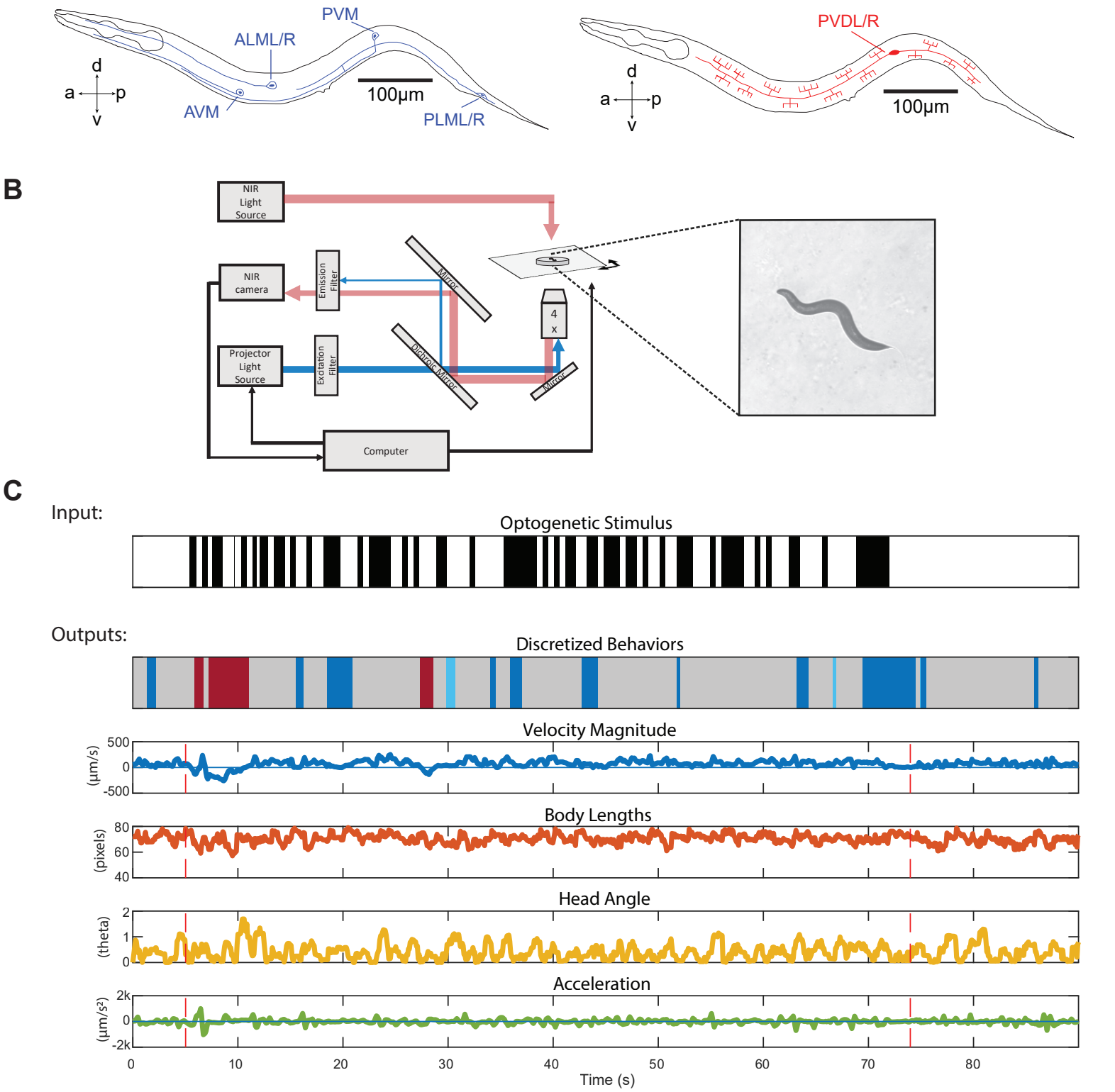
A
PVM
ALML/R
AVM
PLML/R
100µm
d
a
p
v
PVDL/R
B
NIR Light Source
NIR camera
Emission Filter
Mirror
4 x
Projector Light Source
Excitation Filter
Dichroic Mirror
Mirror
Computer
C
Input:
Optogenetic Stimulus
Outputs:
Discretized Behaviors
Velocity Magnitude
(µm/s)
Body Lengths
(pixels)
Head Angle
(theta)
Acceleration
(µm/s²)
Time (s)
D
Change in Acceleration (µm/s2)
Delay to Output (s)
E
Relative Error
Number of Samples (1,000s of Time-Points)

Figure 2

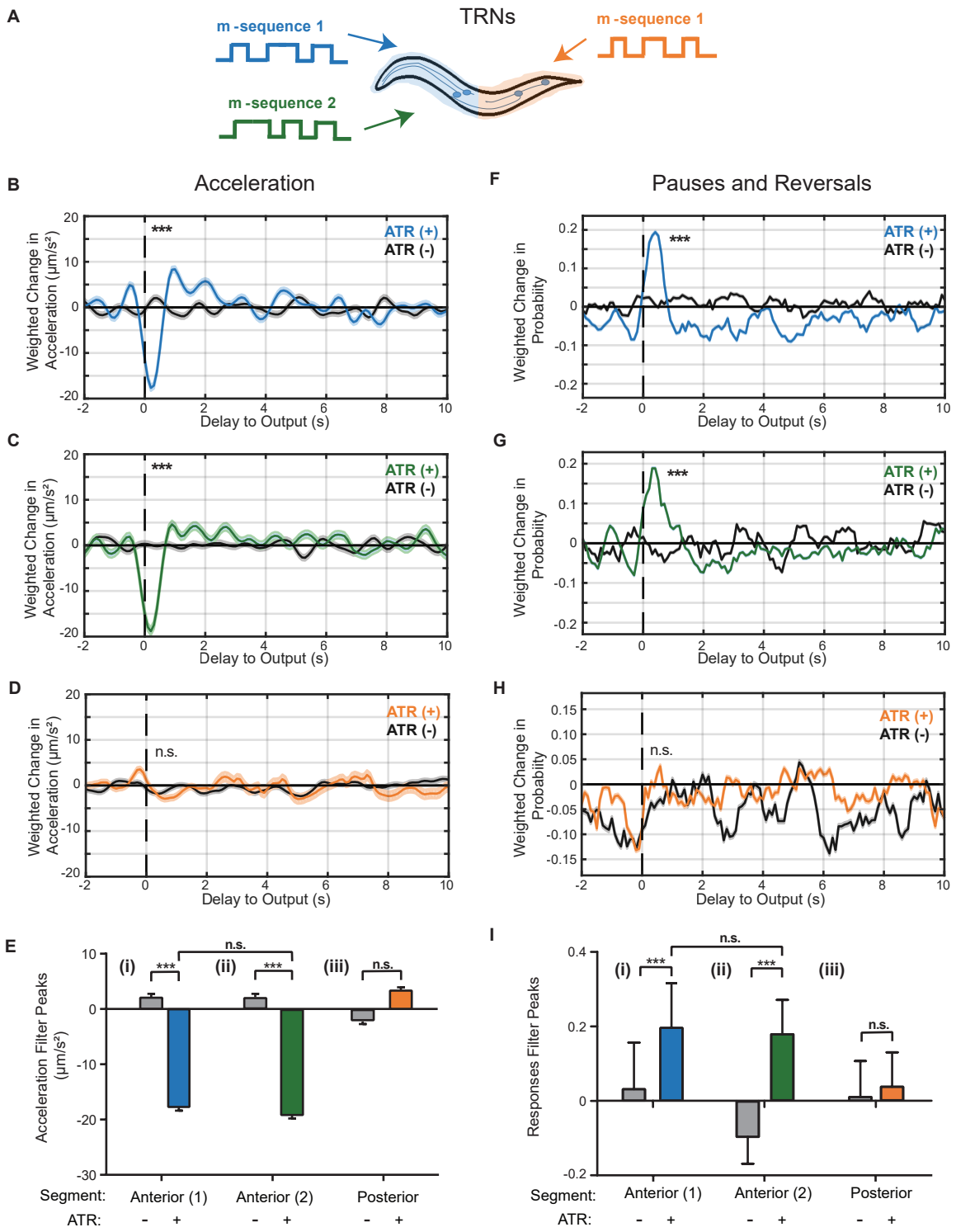
A
m -sequence 1
TRNs
m -sequence 1
m -sequence 2
B
Acceleration
F
Pauses and Reversals
Weighted Change in Acceleration (μm/s²)
Weighted Change in Probability
Delay to Output (s)
ATR (+)
ATR (-)
***
C
G
D
H
n.s.
E
I
Acceleration Filter Peaks (μm/s²)
Responses Filter Peaks
(i)
(ii)
(iii)
Segment:
Anterior (1)
Anterior (2)
Posterior
ATR:

Figure 3

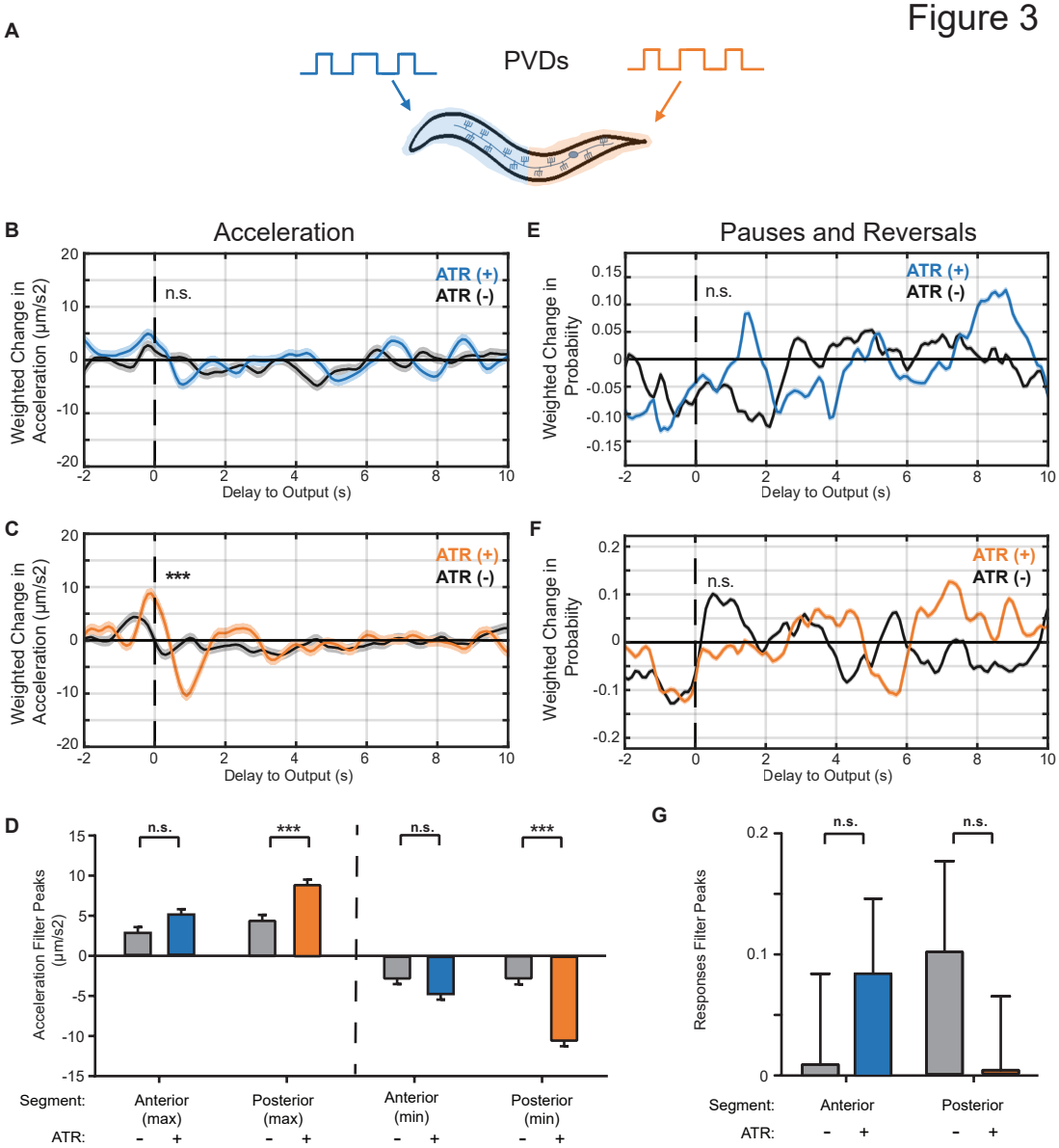
A
PVDs
B
Acceleration
Weighted Change in Acceleration (µm/s2)
n.s.
ATR (+)
ATR (-)
Delay to Output (s)
C
***
E
Pauses and Reversals
Weighted Change in Probability
F
D
Acceleration Filter Peaks (µm/s2)
Segment:
Anterior (max)
Posterior (max)
Anterior (min)
Posterior (min)
ATR:
G
Responses Filter Peaks
Anterior
Posterior

Figure 4

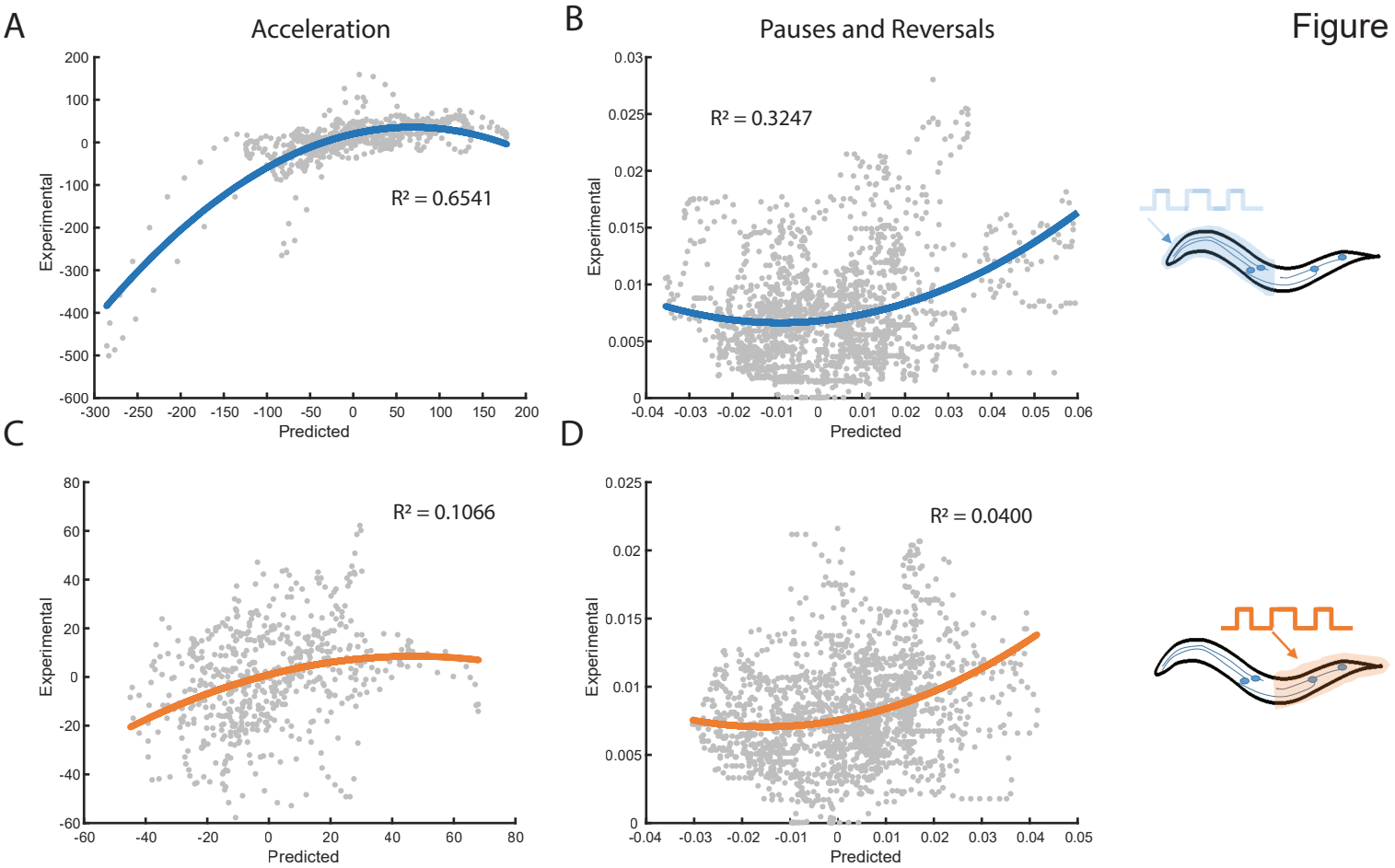
A
Acceleration
R² = 0.6541
Experimental
Predicted
B
Pauses and Reversals
R² = 0.3247
Experimental
Predicted
C
R² = 0.1066
Experimental
Predicted
D
R² = 0.0400
Experimental
Predicted

Figure 5

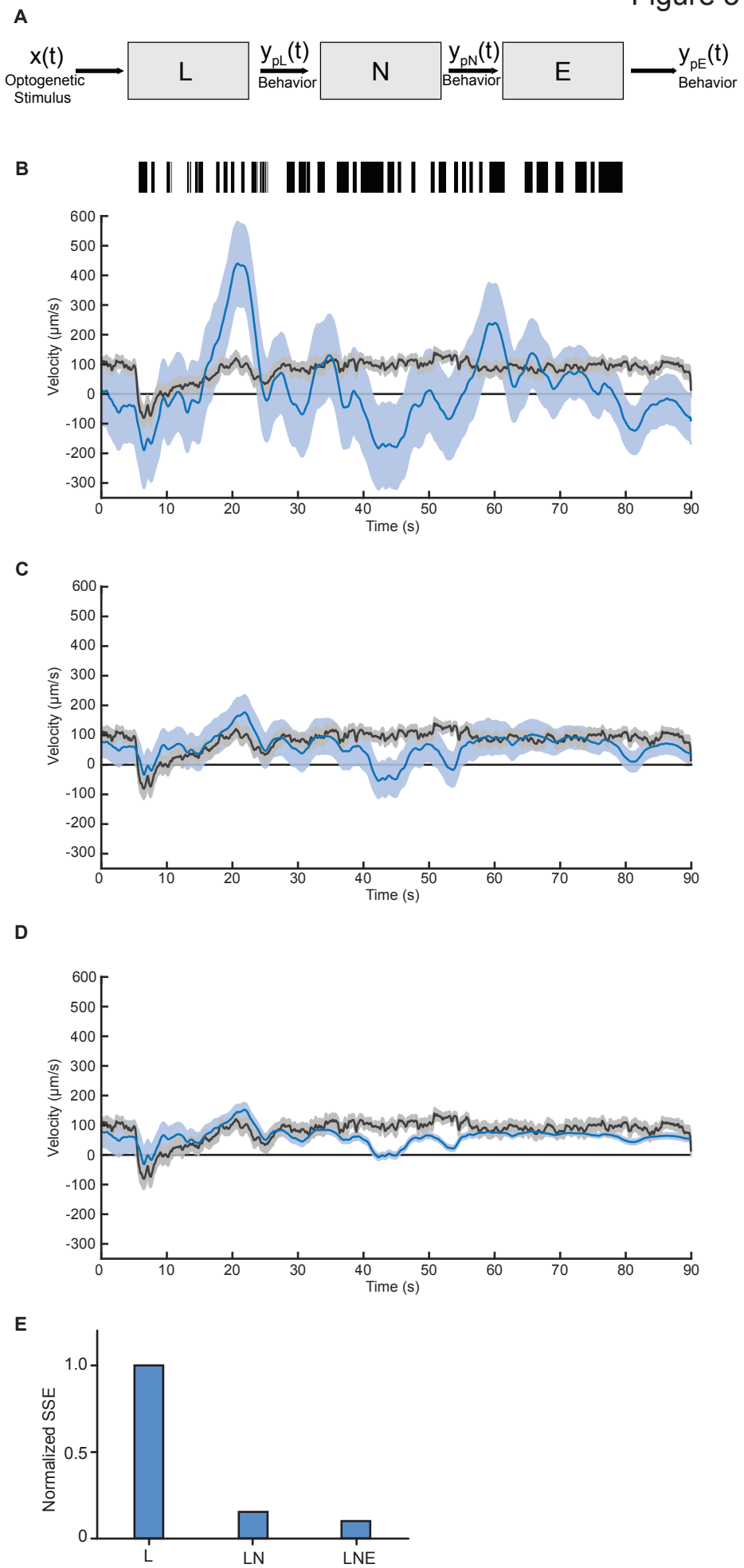
A
x(t)
Optogenetic Stimulus
L
$y_{pL}(t)$
Behavior
N
$y_{pN}(t)$
Behavior
E
$y_{pE}(t)$
Behavior
B
Velocity (μm/s)
Time (s)
C
Velocity (μm/s)
Time (s)
D
Velocity (μm/s)
Time (s)
E
Normalized SSE
L
LN
LNE

Figure 6

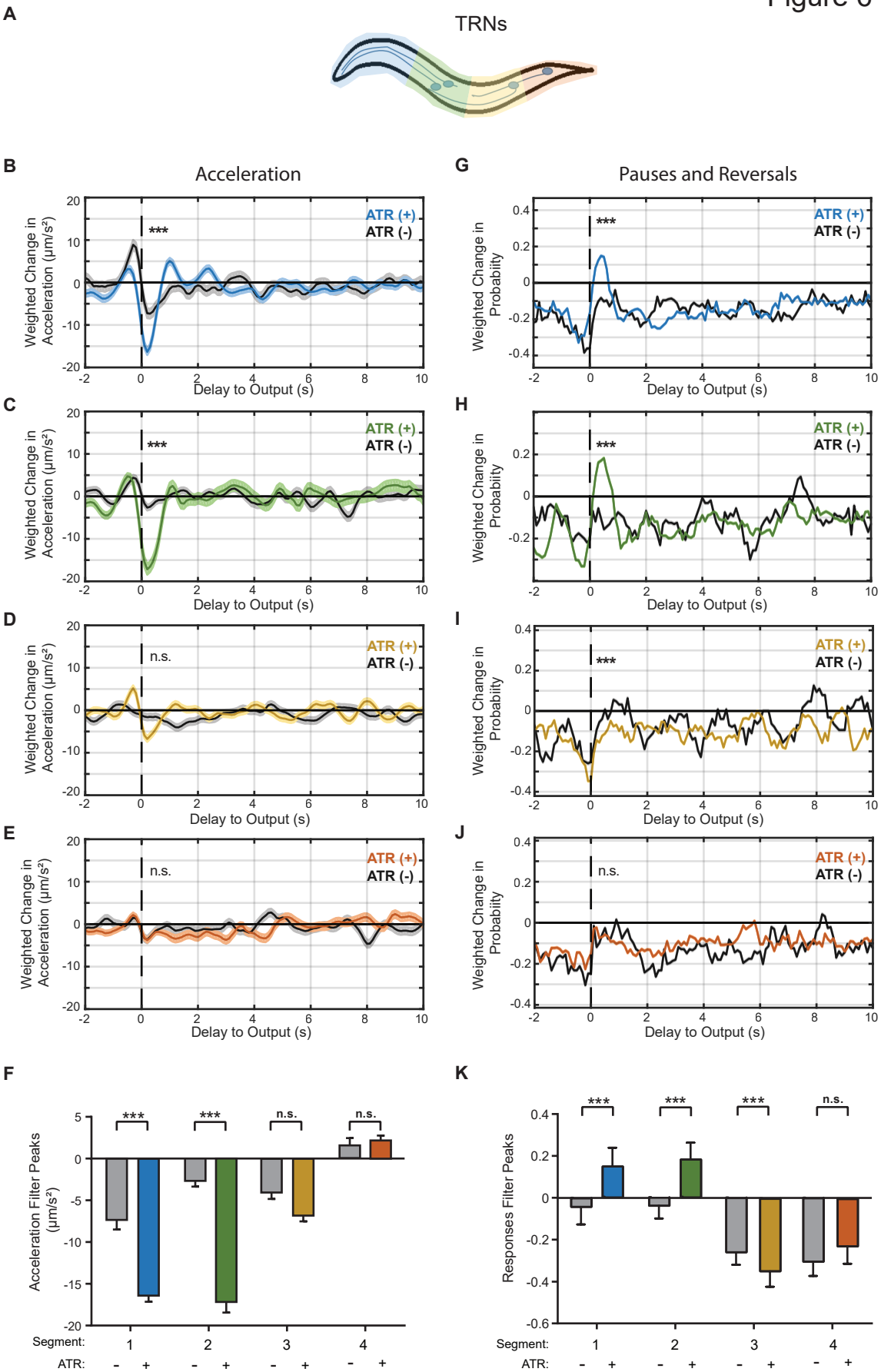
A
TRNs
B
Acceleration
G
Pauses and Reversals
C
D
E
H
I
J
F
K
ATR (+)
ATR (-)
***
n.s.
Weighted Change in Acceleration (μm/s²)
Weighted Change in Probability
Delay to Output (s)
Acceleration Filter Peaks (μm/s²)
Responses Filter Peaks
Segment:
ATR: